ADVANCING EARTH AND SPACE SCIENCES

JGR Earth Surface

RESEARCH ARTICLE
10.1029/2025JF008286

# Measurement of Englacial Velocity Fields With Interferometric Radio Echo Sounders

**Thomas O. Teisberg[1], Dustin M. Schroeder[1,2], Paul T. Summers[3,4], and Mathieu Morlighem[5]**

[1]Department of Electrical Engineering, Stanford University, Stanford, CA, USA, [2]Department of Geophysics, Stanford University, Stanford, CA, USA, [3]School of Earth and Atmospheric Sciences, Georgia Institute of Technology, Atlanta, GA, USA, [4]Department of Marine and Coastal Sciences, Rutgers University, New Brunswick, NJ, USA, [5]Department of Earth Sciences, Dartmouth College, Hanover, NH, USA

**Key Points:**

- Interferometric processing of repeat-pass radio echo sounder data can be used to measure englacial motion
- Sloped layers complicate interpretation of apparent layer motion, but 3D englacial velocity is found by integration from a known boundary
- Englacial velocity measurements can inform estimates of rheology, basal sliding, and mass flux

**Correspondence to:**

T. O. Teisberg,
teisberg@stanford.edu

**Citation:**

Teisberg, T. O., Schroeder, D. M., Summers, P. T., & Morlighem, M. (2025). Measurement of englacial velocity fields with interferometric radio echo sounders. *Journal of Geophysical Research: Earth Surface*, *130*, e2025JF008286. https://doi.org/10.1029/2025JF008286

Received 9 JAN 2025
Accepted 10 MAY 2025

## Abstract

The surface velocity of ice sheets is now measured at high spatial and temporal resolutions by satellite-borne platforms. The availability of this data has enabled rapid progress in both monitoring the evolution of ice sheets and understanding their underlying physical processes. Because the material properties of ice are spatially variable and poorly constrained, however, it is difficult to infer englacial velocity fields from surface velocity alone. Radio echo sounders, also called ice-penetrating radars, can image beneath the surface and resolve englacial layering, commonly assumed to represent isochronal surfaces. In limited settings, interferometric measurements of these englacial layers have also been used to infer vertical velocity within ice sheets, however these applications to date have focused on areas where layers could be assumed to be flat. Here, we develop the mathematical relationships between observed englacial layer deformation and englacial velocity fields, making no assumptions about the shape of the layers and very minimal assumptions about the internal velocity structure. Taking this general approach opens up the possibility of using interferometric radio echo sounding to reconstruct three-dimensional englacial velocity fields at large scale across ice sheets. Potential applications of this method include data-driven estimation of ice rheology, inference of englacial conditions, and estimation of basal sliding. The proposed technique provides more direct constraints on these processes than has previously been available by remote sensing methods and offers the potential to both understand and predict the flow of ice sheets and glaciers.

## Plain Language Summary

The surface flow of ice sheets and glaciers can be observed from satellites, however the movement of ice beneath the surface remains largely unknown. Due to the wide range of material properties of ice, it is difficult to estimate sub-surface velocity from surface measurements. Multiple radio echo sounder measurements at different points in time can be used to measure the motion of internal layers that occur in ice sheets. The motion of these layers has been used to help constrain subsurface velocity, however past work has relied on simplifying assumptions that are only applicable in limited areas of Earth's ice sheets. This paper develops the general mathematic relationships between observed deformation of englacial layers and velocity beneath the ice surface. Enabling more widespread measurements of sub-surface velocity could allow for a better understanding of the physics governing the flow of ice and improve our ability to predict the future evolution of Earth's ice sheets.

## 1. Introduction

Radar interferometry is a well-established technique for precisely measuring the motion of reflecting interfaces over multiple observations. Airborne and satellite-borne radar systems use interferometric synthetic aperture radar (InSAR) techniques to track surface deformation and map surface topography (Ulaby & Long, 2014). Radio echo sounders (RES), also known as ice-penetrating radars, can also be used for interferometry, tracking the motion of reflecting interfaces within or beneath ice sheets, ice shelves, and glaciers relative to the radar's antennas. In the context of polar ice sheets, this technique was first employed to measure ice shelf melt rates by tracking the apparent motion of the ice-ocean interface with stationary radar systems (Brennan et al., 2014; Corr et al., 2002; Jenkins et al., 2006; Nicholls et al., 2015).

RES imaging of polar ice sheets also reveals semi-continuous englacial horizons, commonly known as layers, the origins and structure of which have been a subject of research since the earliest RES surveys (Gudmandsen, 1975). Most work has focused on the use of layers for dating ice (MacGregor, Fahnestock, Catania, Paden, Prasad Gogineni, et al., 2015) or estimating historical flow patterns (Ross et al., 2020), but it is also possible to monitor the current motion of these layers using interferometric RES (InRES) (Castelletti et al., 2020; Kingslake et al., 2014). Because englacial layers tend to be relatively flat and are being advected with the ice's internal motion, phase changes must be interpreted as the result of both vertical velocity and horizontal advection of the layers, complicating the interpretation of observed vertical deformation measurements from InRES (Young et al., 2018).

Although complicated by internal ice dynamics, InRES measurements of englacial layers are a compelling target for observing englacial motion. The composition, temperature, and crystal fabric all strongly influence the rheology of ice (Kuiper et al., 2020). Because none of these variables are easily observable in situ without drilling an ice core, the internal motion of ice in real-world glaciers remains poorly constrained and difficult to predict. Here we will show that InRES measurements of englacial layer motion provide a remote sensing observable that could be used to constrain englacial motion within glaciers and ice sheets.

The ability to create three-dimensional maps of englacial velocity structure holds the promise to rapidly advance our understanding of ice physics and directly improve ice sheet model initialization. Ice sheet surface velocity is used by large-scale models as a key constraint in inversion-based initializations (Larour et al., 2012), in the estimation of bed topography (Morlighem et al., 2014), and in estimation of ice rheology (Millstein et al., 2022; Riel & Minchew, 2023; Wang et al., 2025). In all of these applications, three-dimensional velocity data could be added in to existing frameworks to reduce uncertainties. Sub-surface velocity measurements also inform estimates of basal sliding velocities, a currently under-determined parameter which may be critical to predicting ice sheet evolution (Dawson et al., 2022).

In this work, we develop a mathematical foundation for connecting InRES-observed englacial layer motion and englacial ice velocity. We show how, with an appropriate survey design, InRES measurements can be used to reconstruct three-dimensional englacial velocity fields, and we discuss the noise sources impacting these measurements and how this should inform RES instrument design. Finally, we present simulated velocity reconstruction experiments and explore potential applications of InRES surveys, including quantitative estimates of ice rheology and basal slip.

### 1.1. Englacial Layering in Radio Echo Sounding

Continuous englacial horizons identified in radio echo sounder data, representing contrasts in the dielectric properties of the ice, have been attributed to a number of physical phenomena including changes in density (only applicable in the near surface), chemical composition, crystal fabric orientation, and inclusions of other materials such as volcanic ash (Siegert, 1999).

Under most interpretations, englacial layers represent isochronal surfaces (Siegert, 1999) and thus their structure has been interpreted to convey information about the flow history of ice by comparison of their shape to forward model results (Gerber et al., 2021; Whillans, 1976). Notably, englacial layers are the product of the entire flow history they have experienced. Thus, there is no one-to-one mapping between a single temporal observation of layer geometry and the contemporaneous flow field (Parrenin & Hindmarsh, 2007).

### 1.2. Prior Work in Radio Echo Sounder Layer Interferometry

The isochronal nature of englacial layers implies that we can treat these layers as material surfaces, meaning that we assume no mass is transported through a layer boundary. If these layers are assumed to be flat or not in relative horizontal motion, then a time series measurement of the vertical motion of a layer provides a measurement of the local vertical velocity within the ice. Note that the no relative horizontal motion criterion requires both that the horizontal velocity is uniform with depth and that the instrument is advected at the same horizontal velocity (Lagrangian measurement), which may be achieved either by tracking the surface velocity (for airborne systems) or by anchoring the instrument to the surface. This is the principle behind using stationary ground-based radar systems, such as the Autonomous Phase-Sensitive Radio Echo Sounder, to measure basal melt on ice shelves (Brennan et al., 2014; Corr et al., 2002; Jenkins et al., 2006; Nicholls et al., 2015).

This use of radar interferometry to measure deformation of englacial layer motion has been extended with ground-based measurements to observe the Raymond effect near ice rises (Kingslake et al., 2014), estimate motion and orientation of dipping layers (Young et al., 2018), and for measurements of firn compaction (Case & Kingslake, 2022).

The technique has also been shown to work with repeat-pass airborne radio echo sounding data (Ariho, 2023; Ariho et al., 2022; Castelletti et al., 2020; Miller et al., 2020). Airborne repeat-pass interferometry generally differs from ground-based measurements in that airborne repeats tend to follow an Eulerian measurement approach, tracking measurement over time at a fixed location, whereas ground-based systems are generally advected with the surface of the ice and thus make Lagrangian measurements. When airborne measurements are collected along surface flow lines, they may be processed from either an Eulerian or Lagrangian perspective, however in this paper we will focus on the Eulerian frame of reference.

In all of these cases, the study design focuses on areas where it is reasonable to expect that either the layers are relatively flat and/or that the variation in horizontal velocity with depth is negligible. These assumptions do not always hold, however, and complex sloping layer geometries can be found that do not match present-day surface velocity fields (Elsworth et al., 2020). Non-zero layer slopes have been identified as a source of ambiguity in such interferometric measurements (Young et al., 2018). Similar to the use of snapshot layer geometry to infer flow history through data-model comparison, inversions can be used to extract velocity data even with sloped layers by imposing sufficient regularizing constraints on the rheology (Summers et al., 2021).

## 2. Interferometric Measurement of Englacial Layer Deformation

We begin by reviewing the measurement of englacial layer deformation with InRES and deriving the relationship between measured layer deformation and the englacial velocity field.

### 2.1. Notation

We use a Cartesian $(x, y, z)$ coordinate system, with $z$ pointing upwards vertically. The velocity field of the ice is represented as $\mathbf{v} = (u, v, w)$. We identify surface quantities with a subscripted $s$, such that surface velocities are represented as $\mathbf{v}_s = (u_s, v_s, w_s)$ and $z_s$ is the $z$ coordinate value at the ice upper surface.

We treat layers as material surfaces, consisting of the same particles of ice at all times. Each layer is defined by a function $l_i(x, y, t)$ such that the phase center of the dielectric contrast occurs along $l_i(x, y, t) - z = 0$ at time $t$, where $i$ is the index of the layer. We generally omit the subscript $i$ for notational simplicity.

InRES measures the vertical deformation of each layer function $\frac{\partial l_i}{\partial t}(x, y)$. Critically, this observed layer vertical motion at a specific location is not, in general, equivalent to the vertical velocity of a particle of ice at that location. As illustrated in Figure 1, horizontal advection of a layer with a non-zero slope produces a non-zero $\frac{\partial l}{\partial t}$ even when there is zero vertical velocity.

When it is convenient, we also introduce a simplified two-dimensional flowline geometry. Here we introduce an approximation that the horizontal velocity vector at any location is equal in direction (but not necessarily in magnitude) to the surface velocity. We represent the scalar relationship between the velocity at depth and the surface velocity as a function $s(x, y, z)$:

$$\begin{aligned} (u, v, w) &= (s(x, y, z)u_s,\ s(x, y, z)v_s,\ w) \\ s(x, y, z = z_s) &= 1 \end{aligned} \tag{1}$$

At any given location, we can equivalently represent this by rotating the coordinate system by an angle $\beta$ about the $z$ axis such that the local $x$ axis, $x_f$, points along the map plane direction of surface flow and the layer slope in this direction is $\alpha$:

$$\begin{aligned} u_f &= \sqrt{u^2 + v^2} \\ \tan\alpha = \nabla l \cdot \frac{\mathbf{v}}{|\mathbf{v}|} &= \frac{u\dfrac{\partial l}{\partial x} + v\dfrac{\partial l}{\partial y}}{u_f} \end{aligned} \tag{2}$$

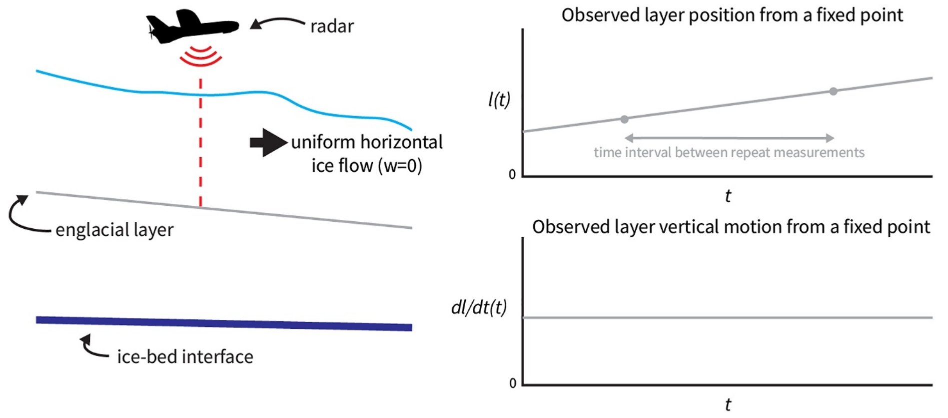


**Figure 1.** Even with zero vertical velocity, horizontal advection of sloped layers produce an apparent vertical motion of the layers from the perspective of a radar system observing from a fixed position.

In this geometry, we use coordinates $(x_f, z)$ with velocity field $(u_f, w)$. We begin with the three-dimensional case and make clear where we use the two-dimensional flowline approximation.

### 2.2. Estimating the Three-Dimensional Englacial Velocity Field

For an ice particle located on a layer boundary described by $l_i(x, y, t)$, the functional $F_i(x, y, z, t) = l_i(x, y, t) - z$ will always evaluate to zero when evaluated along the path of a particle contained in the $i$-th layer since $l_i(x, y, t) = z$ for all particles in this layer. Therefore, the material derivative of this functional will always be zero for particles contained in the layer. From this relationship, we find an expression relating apparent layer motion and horizontal advection:

$$\frac{DF_i}{Dt} = \frac{\partial F_i}{\partial t} + \mathbf{v} \cdot \nabla F_i = \frac{\partial l}{\partial t} + u\frac{\partial l}{\partial x} + v\frac{\partial l}{\partial y} - w = 0 \tag{3}$$

We assume that ice below the firn is incompressible, such that $\nabla \cdot \mathbf{v} = 0$. This implies that $-\frac{\partial w}{\partial z} = \frac{\partial u}{\partial x} + \frac{\partial v}{\partial y}$. Differentiating with respect to $z$ and substituting the result into the incompressibility constraint provides a first-order partial differential equation (PDE) in 3 dimensions ($x$, $y$, and $z$) with two dependent variables ($u$ and $v$):

$$\frac{\partial^2 l}{\partial t \partial z} + u\frac{\partial^2 l}{\partial x \partial z} + \frac{\partial u}{\partial z}\frac{\partial l}{\partial x} + v\frac{\partial^2 l}{\partial y \partial z} + \frac{\partial v}{\partial z}\frac{\partial l}{\partial y} + \frac{\partial v}{\partial y} + \frac{\partial u}{\partial x} = 0 \tag{4}$$

Here we have taken the partial derivative $\frac{\partial^2 l}{\partial t \partial z}$ to be a finite differences approximation of the derivative with respect to $z$ of the $\frac{\partial l_i}{\partial t}$ functions.

All of the partial derivatives of $l$ can be determined from (In)RES radar data, either from single-pass estimation of the layer geometry or, for the time derivatives, estimated by the change between repeat measurements. Unfortunately, Equation 4 is underdetermined, requiring an additional constraint to separate $u$ and $v$.

In this work, we introduce an assumption that the horizontal components of the velocity field are always aligned with the horizontal components of the surface velocity, as described in Section 2.1.

Using Equation 1, the original PDE in Equation 4 can be re-written in terms of a single variable $s(x, y, z)$, representing the scalar relationship between $u$ and $v$ components of the velocity field and the surface velocity.

$$\begin{gathered}\frac{\partial^2 l}{\partial t \partial z} + su_s\frac{\partial^2 l}{\partial x \partial z} + u_s\frac{\partial s}{\partial z}\frac{\partial l}{\partial x} + sv_s\frac{\partial^2 l}{\partial y \partial z} + v_s\frac{\partial s}{\partial z}\frac{\partial l}{\partial y} + s\frac{\partial v_s}{\partial y} + v_s\frac{\partial s}{\partial y} + s\frac{\partial u_s}{\partial x} + u_s\frac{\partial s}{\partial x} = 0 \\ u_s\frac{\partial s}{\partial x} + v_s\frac{\partial s}{\partial y} + \left(u_s\frac{\partial l}{\partial x} + v_s\frac{\partial l}{\partial y}\right)\frac{\partial s}{\partial z} = -\left(u_s\frac{\partial^2 l}{\partial x \partial z} + v_s\frac{\partial^2 l}{\partial y \partial z} + \frac{\partial v_s}{\partial y} + \frac{\partial u_s}{\partial x}\right)s - \frac{\partial^2 l}{\partial t \partial z}\end{gathered} \tag{5}$$

This reduction of the PDE to one dependent variable allows it to be solved by the method of characteristics. The characteristic curves, parameterized by $\tau$, for Equation 5 are defined by:

$$\begin{aligned}\frac{dx}{d\tau} &= u_s\\ \frac{dy}{d\tau} &= v_s\\ \frac{dz}{d\tau} &= u_s\frac{\partial l}{\partial x} + v_s\frac{\partial l}{\partial y}\end{aligned} \tag{6}$$

Because $\frac{dx}{d\tau} = u_s$ and $\frac{dy}{d\tau} = v_s$, the characteristic curves projected onto the x-y plane follow surface flow lines. If the starting point for each characteristic curve is selected to be on a layer, then the characteristic curves are the projection of any surface velocity flow line onto any continuous layer. This is a useful property that can simplify data collection and analysis.

Using the chain rule and our choice of characteristic curves, we find that $\frac{\partial s(\tau)}{\partial \tau}$ is equal to the left hand side of Equation 5:

$$\frac{ds(\tau)}{d\tau} = \frac{\partial s}{\partial x}\frac{\partial x}{\partial \tau} + \frac{\partial s}{\partial y}\frac{\partial y}{\partial \tau} + \frac{\partial s}{\partial z}\frac{\partial z}{\partial \tau} = u_s\frac{\partial s}{\partial x} + v_s\frac{\partial s}{\partial y} + \left(u_s\frac{\partial l}{\partial x} + v_s\frac{\partial l}{\partial y}\right)\frac{\partial s}{\partial z} \tag{7}$$

This allows us to find that the solution to Equation 5 reduces to an ordinary differential equation (ODE) along any characteristic curve, as defined by Equation 6:

$$\frac{ds(\tau)}{d\tau} = -\left(u_s\frac{\partial^2 l}{\partial x\partial z} + v_s\frac{\partial^2 l}{\partial y\partial z} + \frac{\partial v_s}{\partial y} + \frac{\partial u_s}{\partial x}\right)s - \frac{\partial^2 l}{\partial t\partial z} \tag{8}$$

Because the characteristic curve follows a surface flow line, any cross-flow layer slope will be zeroed out by the dot product of the surface velocity with the layer slopes. Thus, this may be further simplified by substituting in the along-flow horizontal velocity $u_f$:

$$\frac{ds}{d\tau} = -\left(u_f\frac{\partial^2 l}{\partial xf\partial z} + \frac{\partial v_s}{\partial y} + \frac{\partial u_s}{\partial x}\right)s - \frac{\partial^2 l}{\partial t\partial z} \tag{9}$$

This solution form implies that it is possible to solve for horizontal velocity by integrating along any surface flow line projection onto any continuous layer. Thus, the input data needed may be acquired from a single flight line, flown twice or more at different times, provided that the flight line follows a surface velocity flow line and that enough layers may be continuously traced to estimate the partial derivatives of observed layer motion in Equation 9.

The ODE tends to be stable if the surface flow field is divergent, which is the case across much of the Antarctic and Greenland Ice Sheets. Stability properties are addressed in more detail in Appendix A.

### 2.3. Boundary Conditions

Solving Equation 9 requires a boundary condition. Since the ODE is solved along each layer, this requires knowing the horizontal velocity somewhere along a continuous section of each layer. Without any approximations, these boundary conditions can only come from ice divides (where the horizontal velocity at all depths is zero) or from in situ borehole measurements. In practice, there may be other sources of boundary conditions. If the layers trace a continuous path to a fast-flowing area or onto an ice shelf, it may be sufficient to assume the horizontal velocity throughout the ice is equal to the surface horizontal velocity, though this final value boundary formulation has implications for ODE stability. In principle, it may also be possible to estimate the transformation matrix for a sufficiently unique feature within the ice, in a manner similar to how feature tracking is used to infer surface velocities by correlation (Zheng et al., 2023). Finally, the zero-slope approximation, discussed in Section 3, may provide alternative boundary conditions.

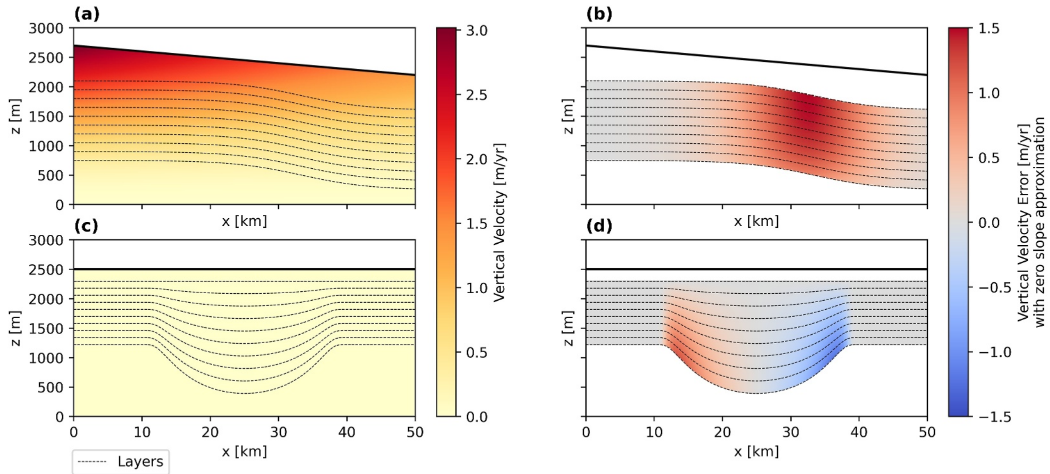


**Figure 2.** Synthetic cases showing the error introduced in vertical velocity estimation by the use of the zero-slope approximation. Dashed lines represent the locations of synthetic layers, constructed to illustrate each error term. The solid black line represents the surface. In the case shown in the top row (a–b), the layers are parallel, but the vertical strain rate is non-zero. Where the layers dip down (non-zero slope), there is an error in the estimated vertical velocity. In the case shown in the bottom row (c–d), the horizontal velocity is uniform throughout (plug flow) but there is variation in the layer slope with depth. Where this variation occurs, a positive or negative vertical velocity is incorrectly estimated.

## 3. Zero Layer Slope Approximation

Up to this point we have drawn a clear distinction between vertical layer motion at a point and vertical velocity of the ice at that location. If, however, layers can be assumed to be flat, this allows for simplifications of the relationship between vertical layer motion at a fixed point and vertical velocity. Substituting the along-flow notation from Equation 2 into Equation 3, we see how the horizontal velocity $u_f$ and layer slope $\alpha$ contribute to the observed layer motion:

$$\frac{\partial l}{\partial t} + u_f \tan \alpha - w = 0 \tag{10}$$

Taking the $z$-derivative to solve for vertical strain rate, we find:

$$\frac{\partial w}{\partial z} = \frac{\partial^2 l}{\partial t \partial z} + \frac{\partial u_f}{\partial z} \tan \alpha + u_f \sec^2(\alpha) \frac{\partial \alpha}{\partial z} \tag{11}$$

The challenge in applying this equation is that the magnitude of the horizontal velocity, $u_f$, is generally unknown, except at the surface. If we neglect the terms involving the horizontal velocity (e.g., by assuming that $\alpha = 0$ for all layers), then we can view any non-zero values of the latter two terms of Equation 11 as error terms. Illustrations of the effects of these two error terms are shown in Figure 2.

In this paper, all measurements are taken to be in an Eulerian frame of reference, however we briefly depart from this convention to note that the error behavior is notably different from a Lagrangian measurement, such as one taken from an instrument anchored to the ice surface. From a Lagrangian reference, the along-flow velocity $u_f$ in the $u_f \sec^2(\alpha) \frac{\partial \alpha}{\partial z}$ would be replaced by the relative motion between the radar platform and the englacial interface. In a Lagrangian measurement, this error term is thus reduced by the horizontal velocity of the radar across the surface. For a more detailed treatment of observed layer motion from a Lagrangian perspective, we refer to Young et al. (2018).

In general, these errors can only be geometrically corrected if a full three-dimensional model of both the layer geometry and the horizontal velocity are known. For the purposes of estimating vertical strain rate, the latter requirement is, presumably, never satisfied. If, however, the goal is to measure melt rates on an ice shelf or another location where the horizontal velocity may be assumed uniform with depth, then geometric corrections, as discussed in Young et al. (2018), are sufficient even if layer slopes cannot be assumed to be zero. The magnitude of potential errors from the zero-slope approximation can be estimated from a simple ice-sheet model. An example of model-derived error estimation is shown in Appendix B.

### 3.1. Interpolation Between Zero Layer Slope Areas

Assuming some noise in the measurements, errors will accumulate as Equation 9 is integrated from a boundary condition, so it is desirable to find areas of known horizontal velocity along the path to avoid long stretches of integrating error. The zero-slope approximation may offer one approach to finding the horizontal velocity in some locations.

If the layer slopes are zero (as, as discussed in Appendix B, very close to zero), then Equation 11 may be used to find the vertical strain rate without integration. If a top or bottom surface boundary condition for horizontal velocity is known, the vertical strain rates may be integrated using conservation of mass to find horizontal velocity through the ice column. If some areas along a flow line can be identified where Equation 11 can be used independently to find horizontal and vertical velocity, these values may serve as boundary conditions for integrating Equation 9.

## 4. Radar Measurement Model

Coherent radio echo sounder systems measure reflections of a transmitted wave off of dielectric contrasts, including englacial layers (Brennan et al., 2014). Assuming that one reflection dominates the return in a given range cell, the phase of the returned signal $\phi_0$ contains sub-range-cell information about the distance to the phase center of the reflecting interface (Brennan et al., 2014). Two spatially coincident measurements separated by an offset time can be interfered to measure the relative phase $\Delta\phi = \phi_1 - \phi_0$, where $\phi_1$ is the phase measured on the second measurement from the same location at a later time. This relative phase contains a signal related to the motion of the target between the two acquisition times:

$$\Delta\phi = \frac{-f_c\sqrt{\epsilon_r}4\pi}{c}\Delta R + \phi_{\text{noise}} \tag{12}$$

In this relationship, $f_c$ is the radar center frequency, $\epsilon_r$ is the relative permittivity of the medium of propagation, $c$ is the speed of light in vacuum, $\Delta R$ is the observed change in range to the layer interface, and $\phi_{\text{noise}}$ is the combined contribution of thermal noise at the time of each measurement. Because we are considering only relative motion beneath the firn, we can assume $\epsilon_r$ to be a constant (see Section 4.4 for more detail).

Due to geometric uncertainties in the sensor location (repeat pass misalignment) and the layer phase center (off-nadir reflections due to sloped layers), the observed change in range is assumed to contain some noise, which will be discussed, along with the previously mentioned thermal noise, in Section 4.1.

$$\Delta R(x, y, \Delta t) = l(x, y, t + \Delta t) - l(x, y, t) - \Delta R_{\text{error}} \tag{13}$$

Neglecting the error terms for now, the radar system observes layer deformation as:

$$\frac{\partial l}{\partial t}(x, y) \approx \frac{\Delta R(x, y, \Delta t)}{\Delta t} \tag{14}$$

### 4.1. Measurement Error Sources

We consider two general classes of measurement error, each of which may impact retrievals of englacial velocities and strain rates. First, thermal noise in the radar system impacts the accuracy with which we may measure the interferometric phase. The variance of the interferometric phase noise due to thermal noise is approximately the inverse of the system signal-to-noise ratio (SNR, Ulaby & Long, 2014).

$$\begin{gathered}\Delta\phi = \frac{-f_c\sqrt{\epsilon_r}4\pi}{c}\Delta R + \phi_{\text{noise}} \\ \text{Var}(\phi_{\text{noise}}) \approx \frac{1}{\text{SNR}}\end{gathered} \tag{15}$$

10.1029/2025JF008286

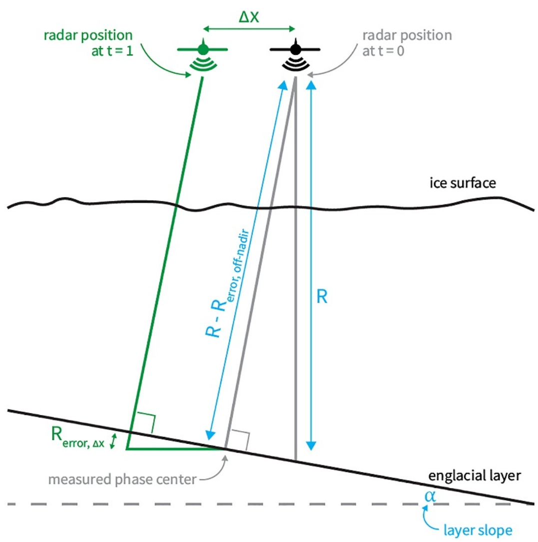


**Figure 3.** Conceptual geometry (not to scale) of a cross-track off-nadir reflection changing the measured phase to a layer with a non-zero cross-track slope (in blue) and the effects of cross-track offset of the two measurements (in green). Note that ray path changes due to the change in relative permittivity between air and ice are not shown here because we assume phases are referenced to a reflection beneath the firn.

A second kind of "noise" results from unknown or unintended variations in the measurement geometry, resulting in measuring a change in range between two points not exactly equal to the intended points. This may arise from three issues: (a) off-nadir reflections due to sloped layer surfaces, (b) variations in the position of the radar between the two measurement times, and (c) constant phase offsets introduced by uncertainty in measuring the surface or bed interface locations. We consider each of these below.

### 4.2. Off-Nadir Reflections From Non-Zero Layer Slopes

Typical airborne radio echo sounding systems have a relatively large antenna footprint. In the along-track track direction, synthetic-aperture focusing can be used to create a narrow effective along-track antenna footprint; however, the cross-track antenna footprint remains large (Culberg & Schroeder, 2020). If the layers being imaged have a non-zero cross-track slope and are largely flat, specular reflectors, as we expect them to be, the phase center of the reflection may not be at nadir. Given a wide cross-track antenna footprint and a gently sloping layer, the measured distance will generally be along the path from the antenna that makes a right angle with the layer, as shown in Figure 3 and represented by the term $R_{\text{error, off-nadir}}$:

$$R_{\text{error, off-nadir}} = R(1 - \cos \alpha) \tag{16}$$

Neglecting any cross-track advection of this layer (a safe assumption along a flow line), the contributed error to the interferometric range estimate is:

$$\Delta R_{\text{error, off-nadir}} = \Delta R(1 - \cos \alpha) \tag{17}$$

A consequence of assuming that the phase center of the reflection is along the ray path perpendicular to the layer is that pointing errors (as a result of antenna calibration issues or bank angle of the aircraft) will have little impact on the distance to the phase center. As the steering angle of the antenna or array increases, the antenna's main lobe may shift far enough that the power return from layers decreases significantly. Assuming largely flat layers, these issues will largely manifest as a decrease in SNR rather than an incorrectly measured phase center.

We have assumed here that the radar instrument has no way of estimating the cross-track layer slope. If the radar system is equipped with a cross-track antenna array, phased-array beamforming may be used to estimate this layer slope (Holschuh et al., 2020). Alternatively, if additional lines are flown perpendicular to the main track, these measurements may be used to estimate the cross-track layer slopes, usually with effective aperture sizes much larger than are feasible with a cross-track array (Castelletti et al., 2019). With known cross-track layer slopes, this error term can be fully corrected.

### 4.3. Radar Instrument Offset Between Measurements

Although efforts should be made to repeat the measured flight line as precisely as possible, some offset between the measurement locations is inevitable. There are numerous factors, including autopilot capabilities, weather, and real-time positioning accuracy, which may impact the precision of repeat flights. Generally speaking, however, reconstructing the true flight lines is an easier problem. By post-processing GNSS data with Precise Point Positioning, sub-meter accuracy can generally be obtained (Gurturk & Soycan, 2022). We will assume that, after post-processing, flight line positions are known to within a fraction of a wavelength (typical wavelengths for RES systems are around 1–5 m) and uncertainty in the actual recorded positions can be ignored.

Any vertical offset is compensated for by phase referencing to an englacial reflector, as previously discussed. Assuming the exact flight paths are known after the fact, measurements can be aligned and interpolated to eliminate any along-track offsets. This leaves only cross-track offsets in the radar position, a situation illustrated by the green annotations in Figure 3.

For a cross-track offset $\Delta x$, the contributed error term is:

$$\Delta R_{\text{error, offset}} = \Delta x \sin \alpha \tag{18}$$

As with the off-nadir reflections, we note that this error term becomes zero if the layers are flat ($\alpha = 0$) and can corrected if the cross-track layers slopes are known, for example, by a cross-track radar array or by performing cross-over flights perpendicular to the main flight line.

### 4.4. Difficulty of Absolutely Referencing Layer Motion

The propagation velocity of radio waves is inversely proportional to the square root of the relative permittivity in a non-magnetic material (Allison et al., 2019). For most purposes, it is safe to assume that the speed of light in glacier ice is a known quantity (Robin, 1975). In the firn, however, unknown compaction properties complicate this (Medley et al., 2015). As a result, it is difficult to absolutely calibrate the reflection distance of a radar system within the first 10s of meters of an ice sheet in the accumulation zone. While this uncertainty is generally small for estimating the depth of a reflector buried in 100s or 1,000s of meters of ice, for a relative position measurement, it cannot be easily ignored. Given the difficulty to quantifying changes in the firn over time, this effectively introduces an unknown range offset between the measurements at the same location but spaced apart in time. As a result, we assume that the interferometric phase of two measurements beneath a firn layer spaced apart in time has some unknown constant offset.

In some cases, the ice-bed interface may provide a reliable reference point, however uncertainties exist here as well. In some cases, the apparent ice-bed interface may also change between acquisitions due to any combination of changes in subglacial water, erosion of the bed, or motion of the solid earth (Vaňková et al., 2018; Wild et al., 2019). Additionally, the ice-bed interface is generally rougher than the englacial layer interfaces. This roughness increases the impact of sensor location offset between the two measurements on interferometric phase (Scanlan et al., 2020). This scenario is similar to aircraft-borne InSAR error analysis (see Chapter 15, Ulaby & Long, 2014).

The amount of uncertainty introduced by either changes in the apparent ice-bed reflection or the firn (depending on your choice of reference) will be highly dependent on the local context. Deep interior regions with flat, frozen beds would likely have minimal uncertainty added by the bed. Areas in the ablation zone where no firn would exist are likely to be similarly low uncertainty using the radar location as the reference point.

In any case, we note that any offset introduced by unknown changes in the firn creates a constant offset in the range measurement for each reflection between two separate measurements. This is important because it means that the vertical spatial derivative of the layer motion can be observed without impact from this error source. That is to say that $\frac{\partial^2 l}{\partial t \partial z}$ can be observed even if $\frac{\partial l}{\partial t}$ is considered unreliable due to unknown firn or bed changes.

As a result, solutions to Equation 9 provide estimates of horizontal velocity which are unaffected by this source of uncertainty, provided that the boundary conditions are also unaffected. Retrievals of vertical velocity from horizontal velocity using Equation 3 depend on $\frac{\partial l}{\partial t}$ and thus are impacted by this error source. The error is canceled out if one is solving only for the vertical strain rate.

### 4.5. Phase Wrapping and Layer Alignment

A final class of error to consider are discrete phase estimation errors, resulting either from phase wrapping of a single target (motion exceeding half a wavelength without correction) or from misalignment of radargrams (incorrectly computing the phase difference between different layers across the two snapshots in time). While avoiding these errors will be an important consideration in building software pipelines for this analysis, they are unlikely to be major obstacles. Because this work looks at tracing the phase differences across long continuous reflectors, mismatched layer pairs and phase wrapping issues should both be relatively easy to spot in processed data. Interferometric RES systems are generally relatively less impacted by phase wrapping as compared to satellite-borne InSAR as a result of their higher fractional bandwidths (Hayes & Gough, 2008). There is also an extensive literature on phase unwrapping in InSAR that can be readily applied to interferometric RES (Yu et al., 2019).

## 5. Applications and Examples

To demonstrate potential applications of this technique, we show several numerical examples using synthetically generated flowline models. The first set of examples highlights the potential of this technique to make in situ estimates of ice rheology, even in grounded ice. We compare three synthetic glaciers with identical surface expressions but different values of the flow exponent in Glen's flow law (W. Glen, 1952; J. Glen, 1958) and show that the flow law exponent can be retrieved from each. We also consider a spatially variable rheology, where the lower parts of the ice column are made up of Eemian ice, represented as a "softer" material (Kuiper et al., 2020; Paterson, 1991).

The second example explores a rapid transition from frozen to sliding, such as what might be seen at the onset location of an ice stream (Mantelli et al., 2019). Although the method does not directly estimate basal velocity, this example shows how seeing horizontal velocity in the lower layers can make a frozen to sliding transition easily apparent. We also consider the impact of temporal changes and show how estimated englacial velocity can be used to determine if the layer geometry reflects steady-state flow (Holschuh et al., 2017; Parrenin & Hindmarsh, 2007). This approach opens the possibility of quantitatively identifying parts of the ice sheet that may have undergone dynamic changes in the recent past.

All of the examples are built around a two-dimensional flowline model using the shallow ice approximation. The results are based on the method of characteristics approach described in Section 2.2. Measurement noise is ignored for now and addressed in the following section.

### 5.1. Rheology Estimation

We consider three synthetic glacier transects with identical topography and surface velocity. In each case, the exponent in Glen's flow law is varied. The $n = 2$ case is used as a reference with prescribed zero horizontal velocity at the bed. In the other two cases, the basal velocity is set such that the surface velocity is identical to the reference case. The velocity field is assumed to be uniform in time and layers are simulated by advecting offset copies of the surface topography in the velocity field. Interferometric measurements are simulated by advecting the simulated layers by 1 year in the velocity field. In this experiment, no noise is added to the measurements.

In each case, the horizontal velocity is solved by numerically integrating Equation 9 along each layer line. Figure 4 shows the results of these integrations at 90 km along the flow line. Although the surface velocities match exactly, the profile of the horizontal velocity with depth varies dramatically as a result of the different rheologies of the three cases.

Effective stress, $\tau_d$, is calculated under the simplifying assumption that the driving stress is due only to gravitational forces and decreases linearly from the bed (see Section 8.2, Cuffey & Paterson, 2010):

$$\tau_d = \rho g (H - z) \frac{dS}{dx} \tag{19}$$

where $\rho$ is the density of ice (assumed to be constant), $g$ is the gravitational acceleration, $H(x)$ is the ice thickness, and $S(x)$ is the surface elevation. In all examples shown here, the bed is flat at $z = 0$. Figure 4e uses the horizontal velocities reconstructed by solving the ODE to estimate strain rate and plots effective stress versus strain rate curves, showing how the exponent used in the flow law for each experiment can be readily estimated from the reconstructions.

Recent data-driven rheology estimation techniques have produced interesting results on ice shelves (Millstein et al., 2022; Riel & Minchew, 2023; Wang et al., 2022), however these techniques cannot be easily extended to grounded ice because they rely on assuming that basal drag is negligible in order to infer strain rate from surface velocity alone. By providing a method to infer englacial velocity without making assumptions on basal drag or rheology, the approach we present here would allow these techniques to be extended to grounded ice and a wider class of processes, problems, and questions. This could provide evidence to resolve current discrepancies between the widely used form of Glen's flow law with $n = 3$ and the more variable flow law forms suggested by the new data-driven rheology literature.

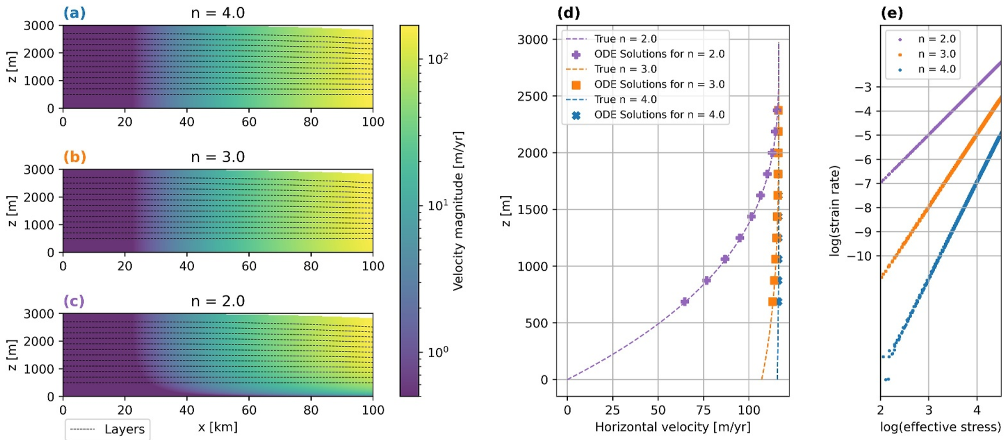


**Figure 4.** Three synthetic flowline models are created with identical surface topography and surface velocity but different rheology in the form of power law relationships with varying exponents. Panels (a)–(c) show horizontal velocity profiles for the three synthetic cases, with black dashed lines indicating the locations of simulated layers. Panel (d) shows profiles of the horizontal velocities at $x = 90$ km, with dashed lines indicating the "true" synthetic values and markers indicating ordinary differential equation (ODE) solutions along the layer lines. Panel (e) shows stress and strain estimated along the ODE solution paths.

### 5.2. Spatially Variable Rheology

A further advantage of retrieving englacial velocities is being able to distinguish the dynamics of different components of the ice column. Temperature, chemical composition, grain size, crystal fabric orientation, and other factors can cause spatially variable ice rheology (Goldsby & Kohlstedt, 2001). Depth-dependent ice rheology, which can currently only be resolved with borehole data, may play an important role in ice sheet dynamics (Seroussi et al., 2013).

As one example, ice from the Last Glacial Period has been identified to be "softer" than Holocene ice (Kuiper et al., 2020). This "softness" can be approximated by an enhancement factor in Glen's flow law (Paterson, 1991).

We modify the $n = 3$ case from the prior experiment to "soften" the ice below 50% fractional ice thickness by an enhancement factor of 3. The basal velocity field is also updated to keep the surface topography and velocity identical to the prior cases. Figure 5b shows the estimated stress versus strain rate scatter plot with points colored by depth. The depth-dependence of the ice rheology is clearly visible.

This concept could be extended to determine the dependence of the stress/strain rate relationship on temperature, ice fabric, or any other variable of interest, allowing ice sheet models to more accurately account for the dependence of rheology on other englacial conditions.

### 5.3. Observing Basal Sliding

While the echo-free zone (Drews et al., 2009) generally prevents InRES techniques from directly measuring basal sliding, velocity measurements deep within the ice can still provide strong constraints on basal velocity. It is generally assumed that fast surface velocities, >50 m/year in Morlighem et al. (2014) for example, are primarily the result of basal sliding and that slow surface velocities are primarily the result of internal deformation. Intermediate speeds, however, may be a combination of factors. Understanding what happens in transitions between slow and fast flow is critical to predicting future sea level rise (Dawson et al., 2022; Mantelli et al., 2019). Basal reflectivity may be used as a proxy for basal conditions (Dawson et al., 2024; Schroeder et al., 2016), but the exact relationship between basal reflectivity and basal conditions contain ambiguities with traditional RES systems (Broome & Schroeder, 2022; Matsuoka, 2011).

In this example, we explore how a rapid basal transition from frozen to sliding may be observed in the lower layers of the ice column. A rapid onset of basal sliding is prescribed in the basal horizontal velocity around 80 km along the flow line. The onset of sliding produces characteristic dips in the simulated layers (more details on the layer simulation follow). Vertical velocity along the flow transect is calculated both by interpolating the results of the

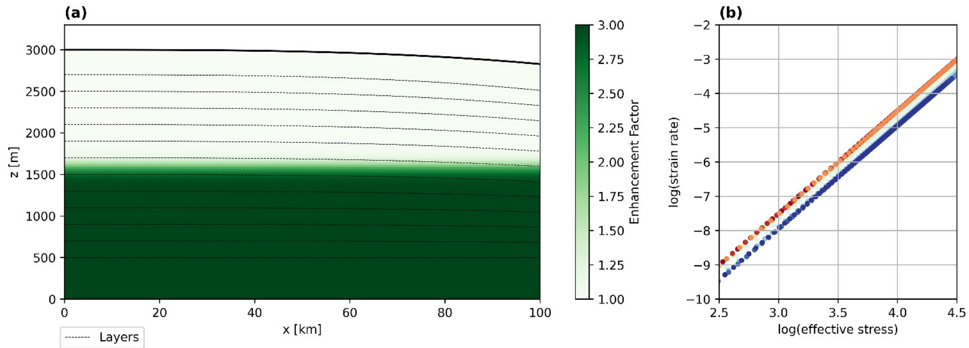


**Figure 5.** (a) A synthetic flowline model with "softer" ice (represented as an enhancement factor of 3) below 1,600 m. (b) The resulting estimated stress versus strain relationship for this depth-dependent rheology. Points in the rheology plot are shaded by depth. The depth-dependence of the enhancement factor is apparent in the higher red line representing ice from the "softer" bottom part of the glacier. Dashed black lines represent layers; the solid black line represents the surface.

ODEs defined by Equation 9 and by applying the zero-slope approximation, as shown in Equation 10. The result from each approach, along with their errors from the true solution, are shown in Figure 6. The sloping layers resulting from the frozen to sliding transition cause errors in the zero-slope approximation solution that can only be corrected with knowledge of the horizontal velocity profile.

Although the simulated layers do not extend to the bed, Figure 7 shows how the lowest layer more clearly shows the true basal velocity profile. How closely the lowest layer matches the basal velocity is primarily determined by how close to the bed the last observable layer is and the local rheology. The relationship between surface velocity and basal velocity is complex and not well understood (Raymond & Gudmundsson, 2005). Englacial velocity measurements would provide a new constraint to improve our understanding of basal sliding, which is critical to understanding ice streams (Mantelli et al., 2019) and predicting future ice mass loss (Dawson et al., 2022).

### 5.4. Identifying Englacial Velocity in Transition

The layers in the above example were simulated by advecting the surface profile by an increasing number of years within the velocity field *with no basal sliding* to form each layer. This layer geometry was then advected within the

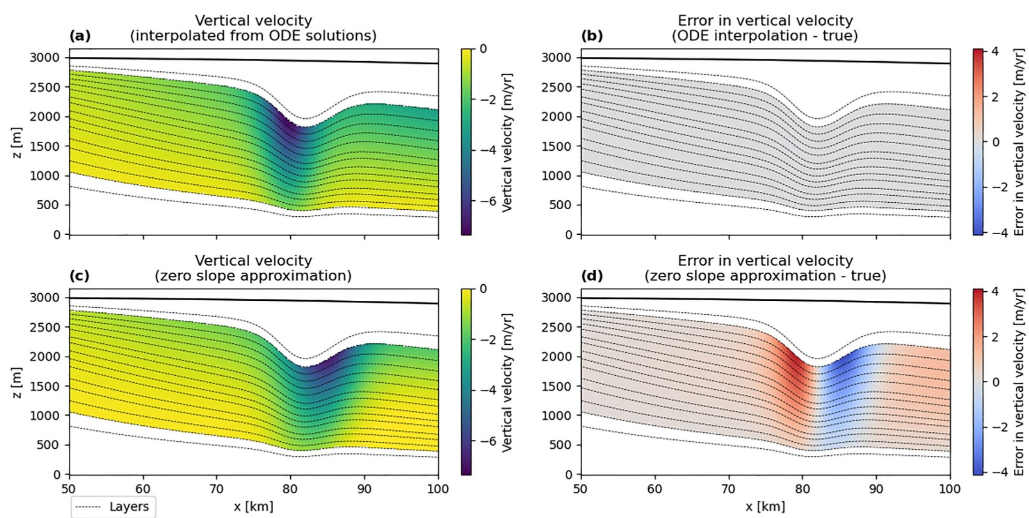


**Figure 6.** Results of solving for vertical velocity in a synthetic frozen-to-sliding transition case. The top plots (a–b) show the results of interpolating the ordinary differential equations along the characteristic curves, which correctly reconstructs the nearly vertical column of increased vertical velocity. The bottom plots (c–d), showing the results of the zero-slope approximation, capture the general trend but distort and shift the vertical velocity profile. The maximum layer dip in this example is less than 7°. Dashed black lines represent layers; the solid black line represents the surface.

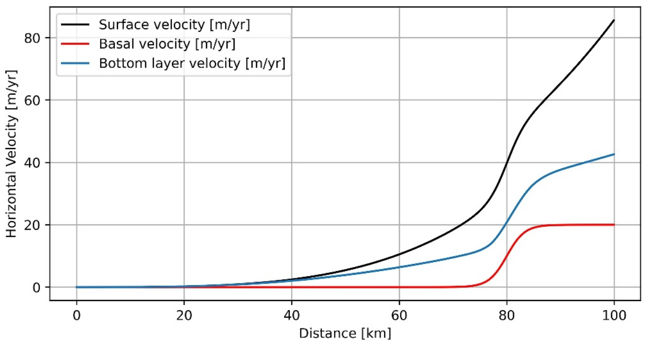


**Figure 7.** Horizontal velocity profiles at the surface, the bed, and the lowest available layer are shown for the same simulated setup as Figure 6. Although basal velocity cannot be directly observed with InRES, the horizontal velocity profiles of layers deep within the ice provide better indicators of basal velocity than surface velocity alone.

velocity field *with* basal sliding for an additional 100 years. As a result, the simulated layers represent a geometry in transition from one steady-state flow regime to another. After reconstructing the englacial velocity profile, the geometry of layers advected only through the current flow profile can be determined. By comparing the slopes of the observed layers to the expected slopes of layers in a steady state flow with the current englacial velocity profile, we can estimate if the current flow field is in steady state, relative to the ages of the observed layers. Figure 8 shows how this layer misalignment analysis reveals the parts of the velocity profile that are not in steady state. This approach may be able to shed light on the flow history of glaciers, especially around areas of rapid transition in velocity, and provides a constraint on ice flow that may predate the satellite record in some cases.

### 5.5. Measurement Noise and Cross-Track Error Simulations

Section 4.1 outlines a model for how measurement noise and uncompensated geometry errors can impact reconstructions of englacial velocity. Starting from the same setup as in Section 5.3, we introduce Gaussian noise in the layer measurements, following Equation 15, and simulate the effects of uncompensated cross-track layer slopes.

We note that care must be taken in specifying the SNR of a radar instrument because the SNR generally increases through a series of post-processing steps, which may include coherent summation, incoherent summation, and focusing. These tasks are commonly split between onboard processing and post-processing, so care must be taken in translating these results between radar systems. For these simulations, we specify an SNR at 10 Hz pulse repetition interval (representative of the effective pulse repetition interval after stacking). We assume a center frequency of 60 MHz.

Due to the multiple terms in Equation 9, which must be approximated by finite differences, directly solving the ODE with noisy inputs is often unstable (see Appendix A) due to the physically unrealistic large derivatives of the layer geometry function. To mitigate this, high-frequency noise is reduced by taking a moving average of the layer depth over a 100-m window.

This filtering process is applied independently on each layer at each time. In reality, each layer is not independent of the others surrounding it. These statistical relationships could conceivably be used in the filtering process, but we neglect this potential optimization for now. For real-world applications, layer-optimized focusing (Castelletti et al., 2019) may be a practical approach to successfully extracting high-SNR radargrams while directly estimating layer slopes.

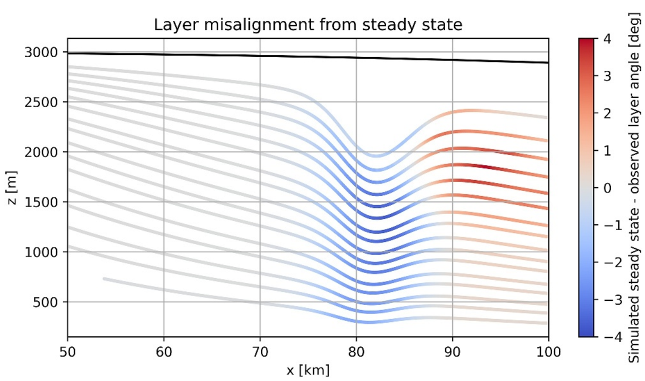


**Figure 8.** Observed layer slopes are compared against layers simulated by advecting within the current velocity profile. The mismatch between these slopes shows areas where the observed layers do not align with the current flow field, suggesting recent changes in the englacial velocity field. Dashed black lines represent layers; the solid black line represents the surface.

The results of solving for horizontal and vertical velocity using the method of characteristics approach with a range of measurement SNRs and uncompensated cross-track slopes are shown in Figure 9. Even under the low SNR and high cross-track slope scenario, the basic patterns of englacial velocity remain clearly visible. Note, however, that this example does not consider any impacts of spatial offsets between repeat measurements.

For horizontal velocity solutions, the error terms accumulate along the ODE solution lines, leading to a striped pattern. For vertical velocity, however, error terms are introduced directly through Equation 3. Note that we do not simulate the effects of unknown changes in the firn (Section 4.4), which would further add to vertical velocity reconstruction error (but not horizontal velocity), unless a suitable correction can be applied.

## 6. Discussion

We have shown that three-dimensional horizontal and vertical englacial velocity profiles may be obtained using interferometric processing of airborne RES data. Successfully achieving this with real-world data collection requires

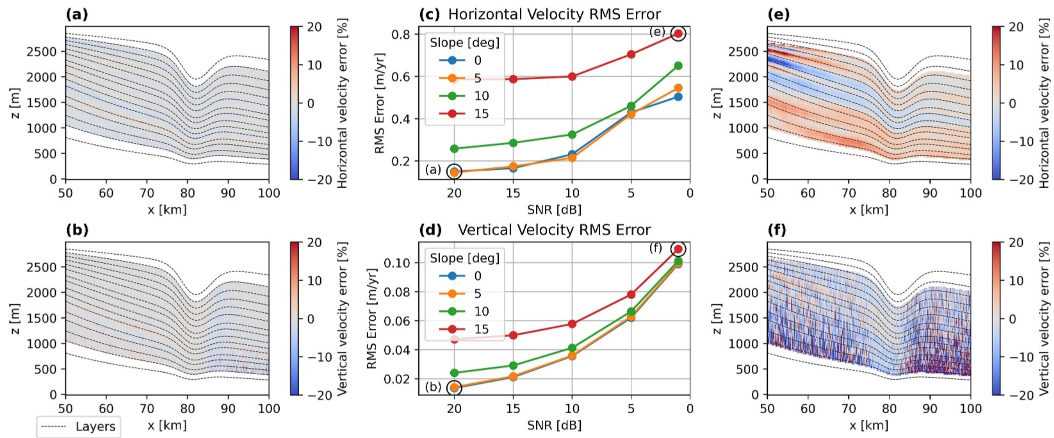


**Figure 9.** (a, b) Example horizontal (a) and vertical (b) englacial velocity reconstruction error at high SNR (25 dB) with zero cross-track slope. (c, d) Comparison of root-mean-square (RMS) error in horizontal (c) and vertical (d) velocity over a range of SNR and cross-track slopes. RMS error is evaluated over the same domain shown in the example figures (a, b, e, f). (e, f) Example horizontal (e) and vertical (f) englacial velocity reconstruction error at very low SNR (1 dB) with 15° cross-track slope. Despite the extreme geometry and high noise levels, the error terms remain relatively small.

careful planning and imposes some requirements on both the radar system and its platform.

Most importantly, englacial velocity reconstruction by the proposed method is only practical if radar data is collected following surface flow lines, where continuously traceable layers are visible and can be traced to a boundary condition where horizontal velocity can be relatively accurately estimated throughout the depth of the ice. Practically, this means an ice divide or, at least, an area of very slow flow close to a divide. Up-to-date surface flow lines must also be known to reasonable precision.

The requirement for continuously traceable layers is likely the strongest constraint on both SNR and bandwidth for radar systems. While bandwidth does not directly enter into SNR as modeled here, the assumption behind Equation 15 is that a single reflection is dominating the return from the relevant range bin, thus the radar bandwidth must be sufficient to fully separate all strong englacial reflectors and the SNR must be sufficient to resolve layers as deep in the ice column as possible.

Knowing the cross-track layer slopes is desirable, though perhaps not a strong requirement depending on the survey objectives. This can be achieved either by flying perpendicular crossing flights or by using a cross-track array (Holschuh et al., 2020). In some cases, this might also be achievable by examining previously collected layer data in the area.

The cross-track layer slopes largely determine the importance of precise re-flights. If the cross-track layer slopes are near zero, there is more tolerance to repeat measurements with some offset. If the cross-track slopes are high, however, either very precise repeat flights are needed or the cross-track slopes need to be mapped very well. In any case, platforms should be equipped to produce sub-wavelength positioning estimates following post-processing, a requirement that should be relatively easy to satisfy with modern GNSS receivers.

Many of these requirements can only be accurately quantified in local context of the layer arrangement, which requires compiling existing radar data or using a pre-made data set, such as the existing radiostratigraphy of Greenland (MacGregor, Fahnestock, Catania, Paden, Prasad Gogineni, et al., 2015) or the results of the currently ongoing AntArchitecture effort (Bingham et al., 2024).

A final survey planning consideration should be the expected stability of the ODE solution, as discussed in Appendix A. The stability criterion for the ODE may be of limited use in many real-world situations where the surface velocity switches between converging and diverging multiple times, in which case the formal criterion cannot offer guarantees either way. Intuitively, however, the stability analysis process can guide away from attempting to apply this technique in areas of strongly converging flow, where the ODEs are unlikely to be stable.

The techniques described in this work offer a pathway to mapping three-dimensional englacial velocity at ice sheet scale. While a theoretical pathway has been laid out, real-world validations are needed to clarify and refine the limits of where and how these approaches may be applied. It is clear that creating an ice sheet-scale velocity map would represent a massive surveying effort. An ice-sheet scale survey pattern would be needed, with repeat measurements needed across all lines at varying intervals, depending on the flow speed of the ice. Effectively, this would transform continent-scale RES surveying from a one-time map making effort to an annual time series product.

The scientific opportunities from building such a time series are extensive. In much the same way that time series surface velocity maps have improved estimates of basal topography (Morlighem et al., 2014), revealed sub-surface hydrology dynamics (Solgaard et al., 2022), improved our understanding of basal sliding (Joughin et al., 2009), provided a means of quantitatively estimating rheology on ice shelves (Millstein et al., 2022), and more, unlocking three-dimensional englacial velocity would have wide-ranging implications for glaciology. This work connects InRES measurements directly to englacial velocity, a field that is already represented but under-constrained in ice sheet models. This provides a direct pathway to incorporating new radar-derived constraints beyond basal topography into numerical models. In addition to direct assimilation into models, englacial velocity maps would allow for quantifying ice rheology across entire ice sheets, not just on ice shelves, and would give a much more direct picture of where basal sliding occurs and how it begins. Englacial velocity maps would also allow for better estimates of mass flux, which would improve mass conservation interpolation-based bed mapping, and a better understanding of how dynamics such as seasonal hydrology cycles impact glacier flow.

Englacial layer structure (without interferometry) has long been used as a record of flow history, but the fact that layers encode the combined effects of hundreds or thousands of years of flow history limits their use for understanding present-day velocity fields. When combined with interferometry to derive current englacial velocity, however, there is an opportunity to compare layer structure with englacial velocity maps to determine if sections of an ice sheet or glacier are in steady state or in a period of transition.

Ice sheet scale englacial velocity maps represent an interesting new potential data source in that they rely on proven and well-understood sensing technology. The basics of radio echo sounding and interferometric radar processing are both extremely well studied. While some instrument advancements may be needed, the primary obstacle to developing three-dimensional velocity maps is logistical, due to the high cost and logistical complications with flying the crewed aircraft used for RES surveys in Antarctica and Greenland. Uncrewed aerial vehicles (UAVs) may provide part of the solution. In addition to reducing the costs associated with airborne surveying, UAVs may simplify the process of collecting repeat lines. If the logistical obstacles can be overcome, englacial velocity maps could rapidly improve the fidelity of ice sheet models and unlock better predictions for the future of Antarctica and Greenland.

## 7. Conclusions

In this paper, we have developed a mathematic framework connecting interferometric radio echo sounding (InRES) observations to subsurface velocity, with minimal assumptions on the internal dynamics of the ice. This approach allows for InRES measurements to be used for englacial velocity estimation across a wide range of possible study sites. We have also illustrated how this general framework compares to the zero slope approximation, and provided some intuition on where the zero slope approximation is or is not applicable.

We have also provided a solution approach that limits the InRES data that must be collected to repeat observations of a single flow line, provided that the flow line is extended to a suitable boundary where the horizontal velocity is known throughout the ice column, most likely an ice divide. Basic error analysis has been provided, although there is much work to be done in extending this to real-world data sets and more complicated processing techniques.

Finally, we have offered some guiding thoughts on the platforms and radar instruments that will be best suited to collecting the repeat measurements needed for InRES processing and englacial velocity estimation.

## Appendix A: Stability of Horizontal Velocity ODE

The ordinary differential equation (ODE) in Equation 8 can be written in the standard form:

10.1029/2025JF008286

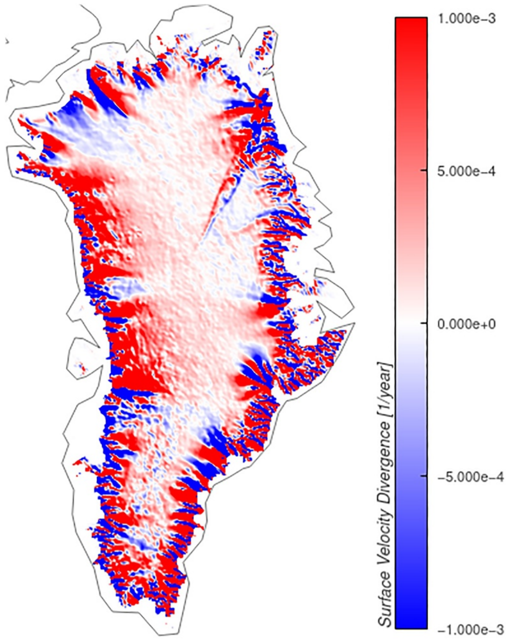


**Figure A1.** Map of the surface velocity divergence in Greenland based on Greenland surface velocity data (A. S. Gardner et al., 2018). Areas in red (positive) are likely to have locally stable behavior of Equation 9.

$$\frac{\partial s}{\partial \tau} = -a(\tau) - sb(\tau) \tag{A1}$$

when $b(\tau) > 0$ for all $\tau$, the ODE is stable, meaning that the solutions for two different initial conditions will vary by no more than the difference in the initial values (Hunt et al., 2009). Equation 9 is stable if the following criterion holds true for all values of $\tau$ in the solution domain:

$$b(\tau) = \underbrace{u_s \frac{\partial^2 l}{\partial x \partial z} + v_s \frac{\partial^2 l}{\partial y \partial z}}_{\text{layer geometry}} + \underbrace{\frac{\partial v_s}{\partial y} + \frac{\partial u_s}{\partial x}}_{\text{surface velocity}} > 0 \tag{A2}$$

If $b(\tau) < 0$ over the entire domain, then Equation 9 is unstable. In cases where $b(\tau)$ changes sign, practically useful bounds are not known to the authors.

This stability condition is a function of surface velocity and layer geometry. Existing radar data, either directly from radargrams or as compiled in radiostratigraphy analyses (MacGregor, Fahnestock, Catania, Paden, Prasad Gogineni, et al., 2015), can be used to estimate the layer geometry component. Surface velocity estimates are widely available from satellite observations.

Investigation of the stability of Equation 9 in specific regions based on all available data is advisable if interferometric radar surveys are being planned.

To develop some intuition about the stability criterion, we separately consider the terms depending on the layer geometry from the terms depending only on the surface velocity, as labeled in Equation A2.

We use a radiostratigraphic compilation across Greenland (MacGregor, Fahnestock, Catania, Paden, Prasad Gogineni, et al., 2015) combined with Greenland surface velocity data from autoRIFT (A. S. Gardner et al., 2018) and bed topography from BedMachine (Morlighem et al., 2014). We apply 5 km standard deviation Gaussian smoothing to the isochrone geometry and surface velocities to minimize measurement artifacts in the data. Within the area where layer geometry is available, we find that the magnitude of the surface velocity divergence term of Equation A2 is greater than the magnitude of the terms depending on the layer geometry about 85% of the time and more than twice the layer geometry terms about 71% of the time. This suggests that, in practice, the layer geometry terms are generally small in comparison to the surface velocity divergence. Thus, for the purpose of gaining intuition about where this technique is most likely to be numerically stable, we may approximate the stability criterion as $\frac{\partial v_s}{\partial y} + \frac{\partial u_s}{\partial x} > 0$, or simply that the surface velocity field is diverging. The divergence of the surface velocity field for Greenland is shown in Figure A1. It is positive throughout most of the interior but varies significantly in faster flowing areas.

## Appendix B: SIA Model to Evaluate Zero Layer Slope Approximation

In order to investigate where the zero layer slope approximation is suitable, we propose considering a shallow ice approximation (SIA, Hutter, 1983) model with a flow exponent of $n = 3$ and the basal horizontal velocity fixed at zero. Greenland surface topography from Morlighem (2022) and surface velocity data generated from A. S. Gardner et al. (2018) are used for this model. The SIA model provides a simulated englacial velocity field, from which we extract the vertical gradients of horizontal velocity. While not strictly a limit, we treat this as an upper bound on plausible vertical gradients of horizontal velocity.

Because estimating the $u_f \sec^2(\alpha)\frac{\partial \alpha}{\partial z}$ term is challenging on an ice sheet scale, we focus on the $\frac{\partial u_f}{\partial z}\tan\alpha$ error term. Using the described SIA model, we find the maximum layer slope $\alpha$ that achieves a given percentage error in vertical strain rate estimation under the zero-slope approximation.

Figure B1 shows the results of evaluating this model at 50% fractional ice thickness for the maximum layer slope that could exist while bounding the error in vertical strain rate to 10%.

We note that the 10% error figure and the 50% ice thickness are both chosen arbitrarily. We also note that this rough model is designed to approximate a case where nothing is known about the rheology or basal conditions. When more is known, a different part of the ice column is being studied, or different error limits apply, this analysis will look different. Our purpose here is to provide an example of our proposed methodology to evaluate if this approximation is suited to a particular task. The evaluation of the suitability of this approximation can only be performed in the full context of a specific study site and a scientific objective.

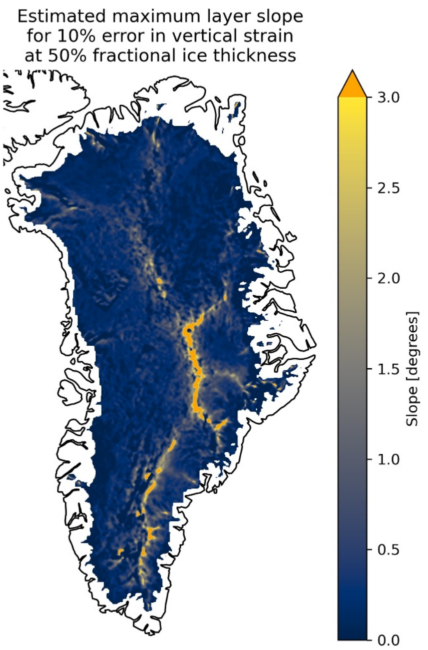


**Figure B1.** Maximum layer slope for 10% error in vertical strain rate when using the zero layer slope approximation, based on an SIA model with $n = 3$ evaluated at 50% fractional ice thickness. Areas in yellow or orange would permit a steeper layer slope, thus making them more feasible as locations to neglect layer slope and apply the zero-slope approximation. Areas in blue likely require additional assumptions on the englacial velocity structure.

While the exact parameters may vary, the map in Figure B1 produces the expected pattern. Slow-flowing areas near ice divides permit much steeper layer slopes for a given percent error in vertical strain rate.

## Data Availability Statement

Greenland surface topography, traced radiostratigraphy, and surface velocity data products are used for the stability analysis in Appendix A. Surface topography data is available from the NSIDC at https://doi.org/10.5067/GMEVBWFLWA7X (Morlighem, 2022). The traced radiostratigraphy data is also available from the NSIDC at https://doi.org/10.5067/UGI2BGTC4QJA (MacGregor, Fahnestock, Catania, Paden, Gogineni, et al., 2015). Greenland surface velocity data was generated using auto-RIFT (A. S. Gardner et al., 2018) and is provided by the NASA MEaSUREs ITS_LIVE project (https://its-live.jpl.nasa.gov/) at https://its-live-data.s3.amazonaws.com/velocity_mosaic/v1/static/GRE_G0120_0000.nc. This data set is alternatively available from the NSIDC at https://doi.org/10.5067/6ii6vw8llwj7 (A. Gardner et al., 2022). All code to reproduce the figures and simulations in this paper are available on GitHub at https://github.com/thomasteisberg/englacial_velocity and archived on Zenodo at https://doi.org/10.5281/zenodo.15191737 (Teisberg et al., 2025).

**Acknowledgments**

The authors would like to thank NASA and the TomKat Center for Sustainable Energy for support in developing this work. We would also like to thank Roland Warner for helpful email conversations in response to early versions of this work. T. O. Teisberg was supported by a NASA FINESST Grant (80NSSC23K0271), the TomKat Center for Sustainable Energy, and Stanford Data Science. Additional support was provided by the Heising-Simons Foundation and the Stanford Institute for Human-Centered Artificial Intelligence. The authors would like to thank the editor, Dr. Jaap Nienhuis, Dr. John Paden, and one anonymous reviewer for their helpful feedback and suggestions.

## References

Allison, P., Archambault, S., Auffenberg, J., Bard, R., Beatty, J., Beheler-Amass, M., et al. (2019). Measurement of the real dielectric permittivity ϵ of glacial ice. *Astroparticle Physics*, *108*, 63–73. https://doi.org/10.1016/j.astropartphys.2019.01.004

Ariho, G. (2023). *Multipass SAR processing for ice sheet vertical velocity and tomography measurements*. Doctoral dissertation. University of Kansas. Retrieved from https://hdl.handle.net/1808/35033

Ariho, G., Paden, J. D., Hoffman, A., Christianson, K. A., & Holschuh, N. (2022). Joint estimation of ice sheet vertical velocity and englacial layer geometry from multipass synthetic aperture radar data. In *2022 IEEE international symposium on phased array systems & technology (PAST)* (pp. 01–05). IEEE. https://doi.org/10.1109/PAST49659.2022.9974985

Bingham, R. G., Bodart, J. A., Cavitte, M. G. P., Chung, A., Sanderson, R. J., Sutter, J. C. R., et al. (2024). Antarctica's internal architecture: Towards a radiostratigraphically-informed age–depth model of the Antarctic ice sheets. https://doi.org/10.5194/egusphere-2024-2593

Brennan, P. V., Lok, L. B., Nicholls, K., & Corr, H. (2014). Phase-sensitive FMCW radar system for high-precision Antarctic ice shelf profile monitoring. *IET Radar, Sonar & Navigation*, *8*(7), 776–786. https://doi.org/10.1049/iet-rsn.2013.0053

Broome, A. L., & Schroeder, D. M. (2022). A radiometrically precise multi-frequency ice-penetrating radar architecture. *IEEE Transactions on Geoscience and Remote Sensing*, *60*, 1–15. https://doi.org/10.1109/TGRS.2021.3099801

Case, E., & Kingslake, J. (2022). Phase-sensitive radar as a tool for measuring firn compaction. *Journal of Glaciology*, *68*(267), 139–152. https://doi.org/10.1017/jog.2021.83

Castelletti, D., Schroeder, D. M., Jordan, T. M., & Young, D. (2020). Permanent scatterers in repeat-pass airborne VHF radar sounder for layer-velocity estimation. *IEEE Geoscience and Remote Sensing Letters*, *1–5*(10), 1766–1770. https://doi.org/10.1109/LGRS.2020.3007514

Castelletti, D., Schroeder, D. M., Mantelli, E., & Hilger, A. (2019). Layer optimized SAR processing and slope estimation in radar sounder data. *Journal of Glaciology*, *65*(254), 983–988. https://doi.org/10.1017/jog.2019.72

Corr, H. F. J., Jenkins, A., Nicholls, K. W., & Doake, C. S. M. (2002). Precise measurement of changes in ice-shelf thickness by phase-sensitive radar to determine basal melt rates. *Geophysical Research Letters*, *29*(8). https://doi.org/10.1029/2001GL014618

Cuffey, K., & Paterson, W. S. B. (2010). *The physics of glaciers* (4th ed. ed.). Butterworth-Heinemann/Elsevier. (OCLC: ocn488732494).

Culberg, R., & Schroeder, D. M. (2020). Firn clutter constraints on the design and performance of orbital radar ice sounders. *IEEE Transactions on Geoscience and Remote Sensing*, *58*(9), 6344–6361. https://doi.org/10.1109/TGRS.2020.2976666

Dawson, E. J., Schroeder, D. M., Chu, W., Mantelli, E., & Seroussi, H. (2022). Ice mass loss sensitivity to the Antarctic ice sheet basal thermal state. *Nature Communications*, *13*(1), 4957. https://doi.org/10.1038/s41467-022-32632-2

Dawson, E. J., Schroeder, D. M., Chu, W., Mantelli, E., & Seroussi, H. (2024). Heterogeneous basal thermal conditions underpinning the Adélie-George V Coast, East Antarctica. *Geophysical Research Letters*, *51*(2), e2023GL105450. https://doi.org/10.1029/2023GL105450

Drews, R., Eisen, O., Weikusat, I., Kipfstuhl, S., Lambrecht, A., Steinhage, D., et al. (2009). Layer disturbances and the radio-echo free zone in ice sheets. *The Cryosphere*, *3*(2), 195–203. https://doi.org/10.5194/tc-3-195-2009

Elsworth, C. W., Schroeder, D. M., & Siegfried, M. R. (2020). Interpreting englacial layer deformation in the presence of complex ice flow history with synthetic radargrams. *Annals of Glaciology*, *61*(81), 206–213. https://doi.org/10.1017/aog.2019.41

Gardner, A., Fahnestock, M., & Scambos, T. (2022). MEaSUREs ITS_LIVE regional glacier and ice sheet surface velocities, version 1 [Dataset]. *NASA National Snow and Ice Data Center Distributed Active Archive Center*. https://doi.org/10.5067/6II6VW8LLWJ7

Gardner, A. S., Moholdt, G., Scambos, T., Fahnstock, M., Ligtenberg, S., van den Broeke, M., & Nilsson, J. (2018). Increased West Antarctic and unchanged East Antarctic ice discharge over the last 7 years. *The Cryosphere*, *12*(2), 521–547. https://doi.org/10.5194/tc-12-521-2018

Gerber, T. A., Hvidberg, C. S., Rasmussen, S. O., Franke, S., Sinnl, G., Grinsted, A., et al. (2021). Upstream flow effects revealed in the EastGRIP ice core using Monte Carlo inversion of a two-dimensional ice-flow model. *The Cryosphere*, *15*(8), 3655–3679. https://doi.org/10.5194/tc-15-3655-2021

Glen, J. (1958). *The flow law of ice: A discussion of the assumptions made in glacier theory, their experimental foundations and consequences*. IAHS.

Glen, W. (1952). Experiments on the deformation of ice. *Journal of Glaciology*, *4*.

Goldsby, D. L., & Kohlstedt, D. L. (2001). Superplastic deformodemation of ice: Experimental observations. *Journal of Geophysical Research*, *106*(B6), 11017–11030. https://doi.org/10.1029/2000JB900336

Gudmandsen, P. (1975). Layer echoes in polar ice sheets. *Journal of Glaciology*, *15*(73), 95–101. https://doi.org/10.3189/S0022143000034304

Gurturk, M., & Soycan, M. (2022). Accuracy assessment of kinematic PPP versus PPK for GNSS flights data processing. *Survey Review*, *54*(382), 48–56. https://doi.org/10.1080/00396265.2020.1865016

Hayes, M., & Gough, P. T. (2008). Interferometric synthetic aperture processing: A comparison of sonar and radar. *Journal of the Acoustical Society of America*, *123*(5), 3907. https://doi.org/10.1121/1.2935898

Holschuh, N., Christianson, K., Paden, J., Alley, R., & Anandakrishnan, S. (2020). Linking postglacial landscapes to glacier dynamics usingswath radar at Thwaites Glacier, Antarctica. *Geology*, *48*(3), 268–272. https://doi.org/10.1130/G46772.1

Holschuh, N., Parizek, B. R., Alley, R. B., & Anandakrishnan, S. (2017). Decoding ice sheet behavior using englacial layer slopes. *Geophysical Research Letters*, *44*(11), 5561–5570. https://doi.org/10.1002/2017GL073417

Hunt, B. R., Lipsman, R. L., Osborn, J. E., Outing, D. A., & Rosenberg, J. M. (2009). Solutions of differential equations. In *Differential equations with mathematica* (3rd ed.). Wiley. Theorem 5.2, Page 52.

Hutter, K. (1983). *Theoretical glaciology: Material science of ice and the mechanics of glaciers and ice sheets*. Springer.

Jenkins, A., Corr, H. F., Nicholls, K. W., Stewart, C. L., & Doake, C. S. (2006). Interactions between ice and ocean observed with phase-sensitive radar near an Antarctic ice-shelf grounding line. *Journal of Glaciology*, *52*(178), 325–346. https://doi.org/10.3189/172756506781828502

Joughin, I., Tulaczyk, S., Bamber, J. L., Blankenship, D., Holt, J. W., Scambos, T., & Vaughan, D. G. (2009). Basal conditions for Pine Island and Thwaites Glaciers, West Antarctica, determined using satellite and airborne data. *Journal of Glaciology*, *55*(190), 245–257. https://doi.org/10.3189/002214309788608705

Kingslake, J., Hindmarsh, R. C. A., Aðalgeirsdóttir, G., Conway, H., Corr, H. F. J., Gillet-Chaulet, F., et al. (2014). Full-depth englacial vertical ice sheet velocities measured using phase-sensitive radar: Measuring englacial ice velocities., *119*(12), 2604–2618. https://doi.org/10.1002/2014JF003275

Kuiper, E.-J. N., Weikusat, I., De Bresser, J. H. P., Jansen, D., Pennock, G. M., & Drury, M. R. (2020). Using a composite flow law to model deformation in the NEEM deep ice core, Greenland – Part 1: The role of grain size and grain size distribution on deformation of the upper 2207 m. *The Cryosphere*, *14*(7), 2429–2448. https://doi.org/10.5194/tc-14-2429-2020

Larour, E., Schiermeier, J., Rignot, E., Seroussi, H., Morlighem, M., & Paden, J. (2012). Sensitivity analysis of Pine Island Glacier ice flow using ISSM and DAKOTA. *Journal of Geophysical Research*, *117*(F2), F02009. https://doi.org/10.1029/2011JF002146

MacGregor, J. A., Fahnestock, M. A., Catania, G. A., Paden, J. D., Gogineni, S. P., Young, S. K., et al. (2015). Radiostratigraphy and age structure of the Greenland Ice Sheet, version 1 [Dataset]. *NASA National Snow and Ice Data Center Distributed Active Archive Center*. https://doi.org/10.5067/UGI2BGTC4QJA

MacGregor, J. A., Fahnestock, M. A., Catania, G. A., Paden, J. D., Prasad Gogineni, S., Young, S. K., et al. (2015). Radiostratigraphy and age structure of the Greenland Ice Sheet. *Journal of Geophysical Research: Earth Surface*, *120*(2), 212–241. https://doi.org/10.1002/2014JF003215

Mantelli, E., Haseloff, M., & Schoof, C. (2019). Ice sheet flow with thermally activated sliding. Part 1: The role of advection. *Proceedings of the Royal Society A: Mathematical, Physical and Engineering Sciences*, *475*(2230), 20190410. https://doi.org/10.1098/rspa.2019.0410

Matsuoka, K. (2011). Pitfalls in radar diagnosis of ice-sheet bed conditions: Lessons from englacial attenuation models: Radar diagnosis of ice-sheet beds. *Geophysical Research Letters*, *38*(5), L05505. https://doi.org/10.1029/2010GL046205

Medley, B., Ligtenberg, S., Joughin, I., Van Den Broeke, M., Gogineni, S., & Nowicki, S. (2015). Antarctic firn compaction rates from repeat-track airborne radar data: I. Methods. *Annals of Glaciology*, *56*(70), 155–166. https://doi.org/10.3189/2015AoG70A203

Miller, B., Ariho, G., Paden, J., & Arnold, E. (2020). Multipass SAR processing for radar depth sounder clutter suppression, tomographic processing, and displacement measurements. In *IGARSS 2020 - 2020 IEEE international geoscience and remote sensing symposium* (pp. 822–825). IEEE. https://doi.org/10.1109/IGARSS39084.2020.9324498

Millstein, J. D., Minchew, B. M., & Pegler, S. S. (2022). Ice viscosity is more sensitive to stress than commonly assumed. *Communications Earth & Environment*, *3*(1), 57. https://doi.org/10.1038/s43247-022-00385-x

Morlighem, M. (2022). IceBridge BedMachine Greenland, version 5 [Dataset]. *NASA National Snow and Ice Data Center Distributed Active Archive Center*. https://doi.org/10.5067/GMEVBWFLWA7X

Morlighem, M., Rignot, E., Mouginot, J., Seroussi, H., & Larour, E. (2014). High-resolution ice-thickness mapping in South Greenland. *Annals of Glaciology*, *55*(67), 64–70. https://doi.org/10.3189/2014AoG67A088

Nicholls, K. W., Corr, H. F., Stewart, C. L., Lok, L. B., Brennan, P. V., & Vaughan, D. G. (2015). A ground-based radar for measuring vertical strain rates and time-varying basal melt rates in ice sheets and shelves. *Journal of Glaciology*, *61*(230), 1079–1087. https://doi.org/10.3189/2015JoG15J073

Parrenin, F., & Hindmarsh, R. (2007). Influence of a non-uniform velocity field on isochrone geometry along a steady flowline of an ice sheet. *Journal of Glaciology*, *53*(183), 612–622. https://doi.org/10.3189/002214307784409298

Paterson, W. (1991). Why ice-age ice is sometimes "soft". *Cold Regions Science and Technology*, *20*(1), 75–98. https://doi.org/10.1016/0165-232X(91)90058-O

Raymond, M. J., & Gudmundsson, G. H. (2005). On the relationship between surface and basal properties on glaciers, ice sheets, and ice streams. *Journal of Geophysical Research*, *110*(B8), 2005JB003681. https://doi.org/10.1029/2005JB003681

Riel, B., & Minchew, B. (2023). Variational inference of ice shelf rheology with physics-informed machine learning. *Journal of Glaciology*, *69*(277), 1167–1186. https://doi.org/10.1017/jog.2023.8

Robin, G. D. Q. (1975). Velocity of radio waves in ice by means of a bore-hole interferometric technique. *Journal of Glaciology*, *15*(73), 151–159. https://doi.org/10.3189/S0022143000034341

Ross, N., Corr, H., & Siegert, M. (2020). Large-scale englacial folding and deep-ice stratigraphy within the West Antarctic Ice Sheet. *The Cryosphere*, *14*(6), 2103–2114. https://doi.org/10.5194/tc-14-2103-2020

Scanlan, K. M., Rutishauser, A., Young, D. A., & Blankenship, D. D. (2020). Interferometric discrimination of cross-track bed clutter in ice-penetrating radar sounding data. *Annals of Glaciology*, *61*(81), 68–73. https://doi.org/10.1017/aog.2020.20

Schroeder, D. M., Seroussi, H., Chu, W., & Young, D. A. (2016). Adaptively constraining radar attenuation and temperature across the Thwaites Glacier catchment using bed echoes. *Journal of Glaciology*, *62*(236), 1075–1082. https://doi.org/10.1017/jog.2016.100

Seroussi, H., Morlighem, M., Rignot, E., Khazendar, A., Larour, E., & Mouginot, J. (2013). Dependence of century-scale projections of the Greenland ice sheet on its thermal regime. *Journal of Glaciology*, *59*(218), 1024–1034. https://doi.org/10.3189/2013JoG13J054

Siegert, M. J. (1999). On the origin, nature and uses of Antarctic ice-sheet radio-echo layering. *Progress in Physical Geography: Earth and Environment*, *23*(2), 159–308. https://doi.org/10.1177/030913339902300201

Solgaard, A. M., Rapp, D., Noël, B. P. Y., & Hvidberg, C. S. (2022). Seasonal patterns of Greenland Ice velocity from sentinel-1 SAR data linked to runoff. *Geophysical Research Letters*, *49*(24), e2022GL100343. https://doi.org/10.1029/2022GL100343

Summers, P. T., Schroeder, D. M., & Siegfried, M. R. (2021). Constraining ice sheet basal sliding and horizontal velocity profiles using a stationary phase sensitive radar sounder. In *2021 IEEE international geoscience and remote sensing symposium IGARSS* (pp. 5524–5527). IEEE. https://doi.org/10.1109/IGARSS47720.2021.9554535

Teisberg, T., Schroeder, D., Summers, P., & Morlighem, M. (2025). thomasteisberg/englacial_velocity: Manuscript revision 1 [Software]. *Zenodo*. https://doi.org/10.5281/zenodo.15191737

Ulaby, F. T., & Long, D. G. (2014). *Microwave radar and radiometric remote sensing*. The University of Michigan Press.

Vaňková, I., Voytenko, D., Nicholls, K. W., Xie, S., Parizek, B. R., & Holland, D. M. (2018). Vertical structure of diurnal englacial hydrology cycle at Helheim Glacier, East Greenland. *Geophysical Research Letters*, *45*(16), 8352–8362. https://doi.org/10.1029/2018GL077869
Wang, Y., Lai, C.-Y., Prior, D. J., & Cowen-Breen, C. (2025). Deep learning the flow law of Antarctic ice shelves. *Science*, *387*(6739), 1219–1224. https://doi.org/10.1126/science.adp3300
Whillans, I. M. (1976). Radio-echo layers and the recent stability of the West Antarctic ice sheet. *Nature*, *264*(5582), 152–155. https://doi.org/10.1038/264152a0
Wild, C. T., Marsh, O. J., & Rack, W. (2019). Differential interferometric synthetic aperture radar for tide modelling in Antarctic ice-shelf grounding zones. *The Cryosphere*, *13*(12), 3171–3191. https://doi.org/10.5194/tc-13-3171-2019
Young, T. J., Schroeder, D. M., Christoffersen, P., Lok, L. B., Nicholls, K. W., Brennan, P. V., et al. (2018). Resolving the internal and basal geometry of ice masses using imaging phase-sensitive radar. *Journal of Glaciology*, *64*(246), 649–660. https://doi.org/10.1017/jog.2018.54
Yu, H., Lan, Y., Yuan, Z., Xu, J., & Lee, H. (2019). Phase unwrapping in InSAR: A review. *IEEE Geoscience and Remote Sensing Magazine*, *7*(1), 40–58. https://doi.org/10.1109/MGRS.2018.2873644
Zheng, W., Bhushan, S., Van Wyk De Vries, M., Kochtitzky, W., Shean, D., Copland, L., et al. (2023). GLAcier feature tracking testkit (GLAFT): A statistically and physically based framework for evaluating glacier velocity products derived from optical satellite image feature tracking. *The Cryosphere*, *17*(9), 4063–4078. https://doi.org/10.5194/tc-17-4063-2023